Electronic Supplementary Information

The Crystallinity Effect of Mesocrystalline $BaZrO_3$ Hollow Nanospheres on Charge Separation for Photocatalysis

Tian-Nan Ye,[a] Miao Xu,[a] Wei Fu,[a] Yi-Yu Cai,[a] Xiao Wei,[a] Kai-Xue Wang,[a] Yong-Nan Zhao,[b] Xin-Hao Li*[a] and Jie-Sheng Chen*[a]

[a] School of Chemistry and Chemical Engineering, Shanghai Jiao Tong University, Shanghai 200240, P. R. China. E-mail: xinhaoli@sjtu.edu.cn; chemcj@sjtu.edu.cn.

[b] Institute of Nanostructured Materials & Tianjin Key Laboratory of Fiber Modification and Functional Fiber, School of Materials Science and Engineering, Tianjin Polytechnic University, Tianjin 300387, P. R. China.

*To whom correspondence should be addressed

Experimental Section

Synthesis: All chemicals in preparing hollow particles were of analytical grade without any purification and readily available. The $BaZrO_3$ samples were prepared by concentrated alkali-assisted hydrothermal method according to our previous work.[S1] In a typical procedure, the stoichiometric amount of $ZrOCl_2 \cdot 8H_2O$ and $Ba(NO_3)_2$ were dissolved in KOH solution to form a suspension. After stirring, the final mixtures were transferred into a Teflon-lined stainless-steel autoclave and heated at 200 °C for 24 h in an electric oven. The white powdery products were centrifuged, washed with distilled water, diluted acetic acid and absolute ethanol for several times. Then, the samples were obtained after being dried in vacuum. The hydrothermal obtained white powder samples were calcined at 600 °C, 800 °C and 1000 °C for 6 h in a muffle furnace. For comparison, the reference $BaZrO_3$ samples were prepared through the Pechini-type process.[S2]

Characterization: Powder X-ray diffraction patterns were recorded on a Bruker D8 Advance X-ray diffractometer with Cu-Kα radiation (λ = 1.5418 Å). The morphology and crystal lattice of samples were characterized by transmission electron microscopy (TEM, JEOL, JEM-2100, with an accelerating voltage of 100 kV), high-resolution transmission electron microscopy (HRTEM, JEOL, JEM-2100, with an accelerating voltage of 200 kV), respectively. Shell thickness and size distributions were evaluated by the TEM images of each sample to obtain statistically significant results. XPS measurements were conducted on a Kratos Axis Ultra DLD spectrometer using a monochromated Al Kα radiation. BET surface areas were determined by physical adsorption of nitrogen at -196 °C in a NOVA 2200e instrument, and samples were degassed at 300 °C for 4 h before experiments. The UV–vis absorption spectra were recorded on a Shimadzu UV-2450 spectrometer. The photoluminescence (PL) spectra were recorded on a QM-4-CW (Photo technology international, Int. USA/CAN).

Photocatalytic reaction: Photocatalytic water splitting was performed in a gas-closed circulation system with a top window Pyrex cell, using 300-W Xe lamp as light source (wavelength 200-1100 nm). The effective area for cell is 40.7 cm^2. Gas produced was analyzed by an online thermal conductivity detector (TCD) gas chromatograph (NaX zeolite column, nitrogen as a carrier gas). In all experiments,

150 mL of deionized water containing 0.05 g of catalyst and the mixed sacrificial agent of 0.25 M Na_2SO_3/0.35 M Na_2S (scavenging the photogenerated holes) were added into reaction cell. The whole system was vacuumed several times before reactions to remove dissolved air. Temperature for all photocatalytic reactions was kept at 15±5 °C. For the photocatalytic degradation of MO, 50 mg of photocatalyst was dispersed into 100 mL of 10 $mg \cdot L^{-1}$ MO aqueous solution in a home-made reactor with a cooling water jacket outside. Prior to light illumination, the suspension was strongly magnetically stirred for 120 mins in the dark for adsorption/desorption equilibrium between the photocatalytic and dyes. During the irradiation, about 4 mL of the suspensions was continually taken from the reaction cell at given time intervals, and then centrifuged to remove the photocatalyst particles. After centrifugation, the UV/Vis spectrum of the supernatant was recorded to monitor the absorption behavior. The characteristic absorption peak of MO at 464 nm was used to determine the extent of its degradation.

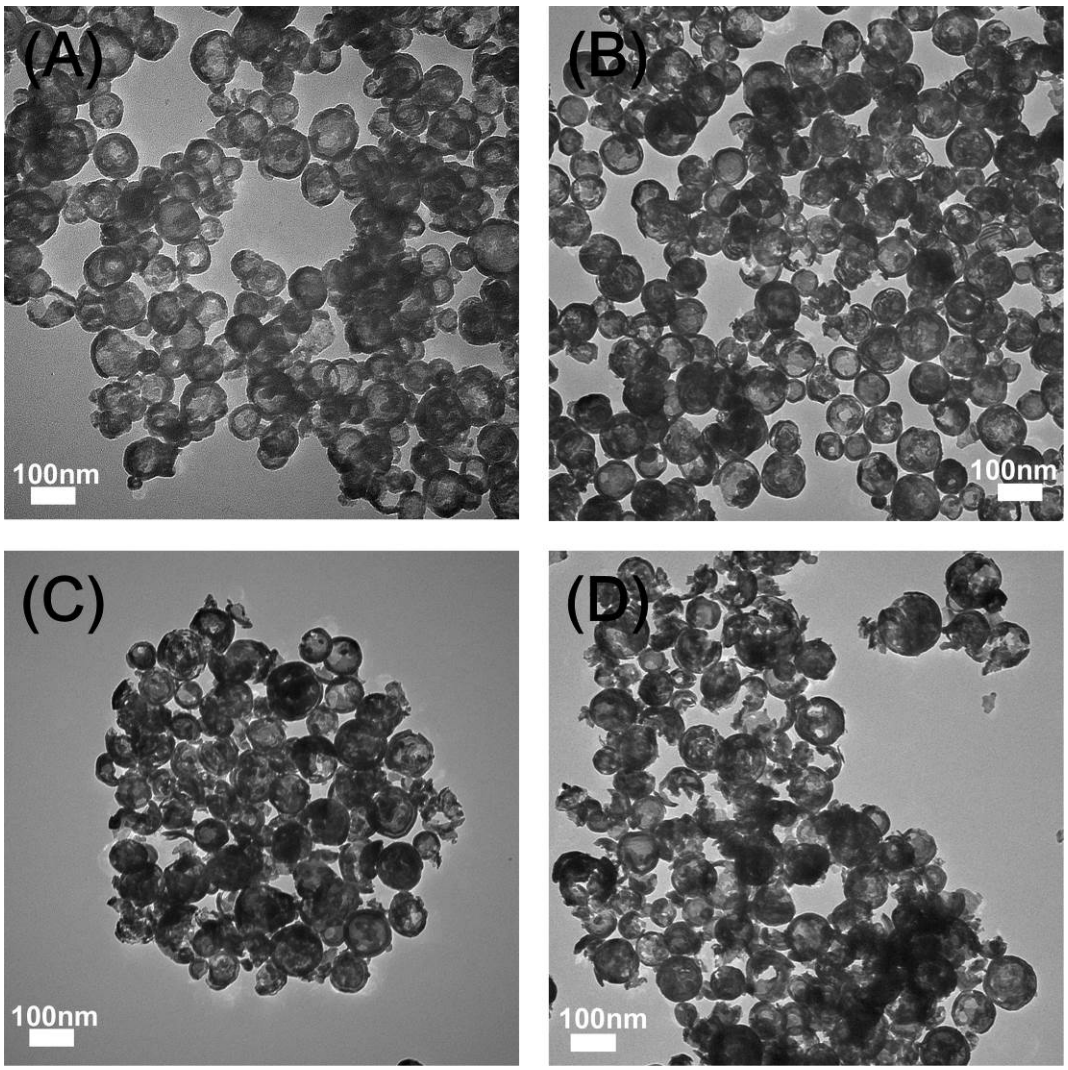

Fig. S1 TEM images of the (A) BZO-mc, (B) BZO-600, (C) BZO-800 and (D) BZO-1000. After calcination, a slight increase in the percentage of the cracked shells was observed.

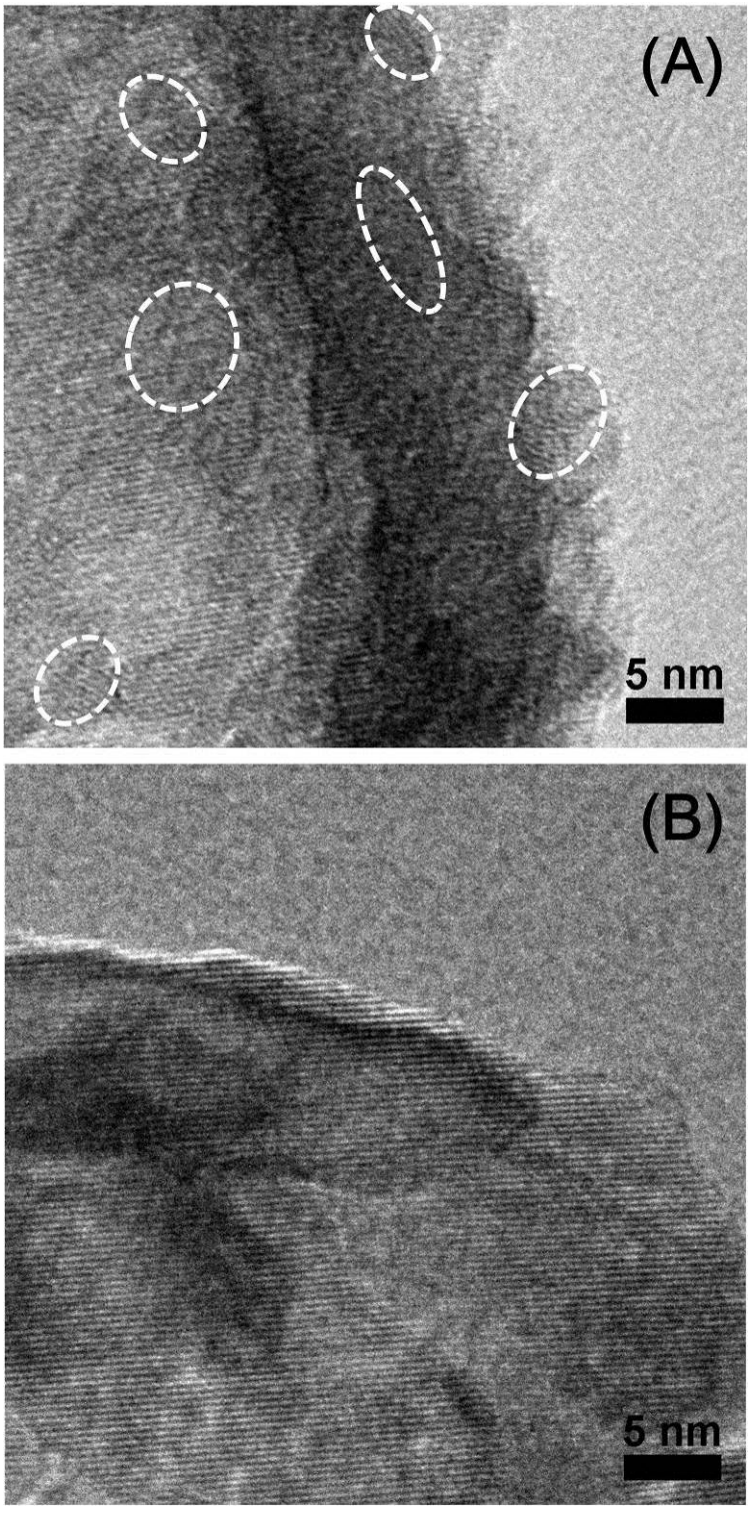

Fig. S2 Large-area HRTEM images of the (A) BZO-mc and (B) BZO-1000. The disordered areas in (A) BZO-mc were marked with white dotted boxes.

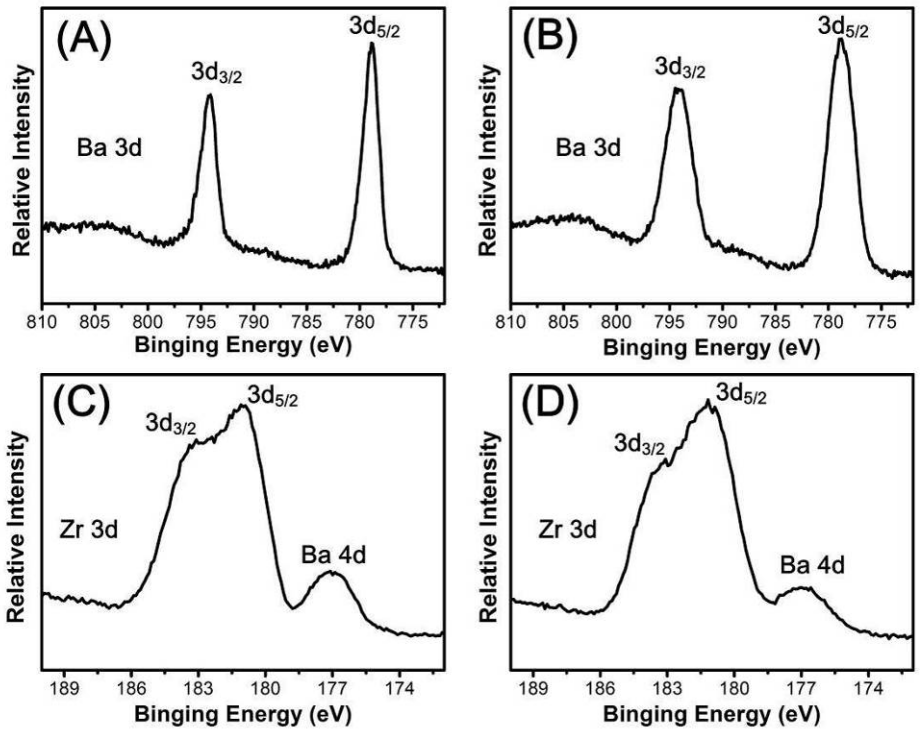

Fig. S3 High-resolution Ba 3d and Zr 3d XPS spectra XPS spectra of the (A, C) BZO-mc, (B, D) BZO-1000. No obvious change was observed in the composition of these samples after calcination as demonstrated by their high-resolution Ba 3d and Zr 3d XPS spectra.

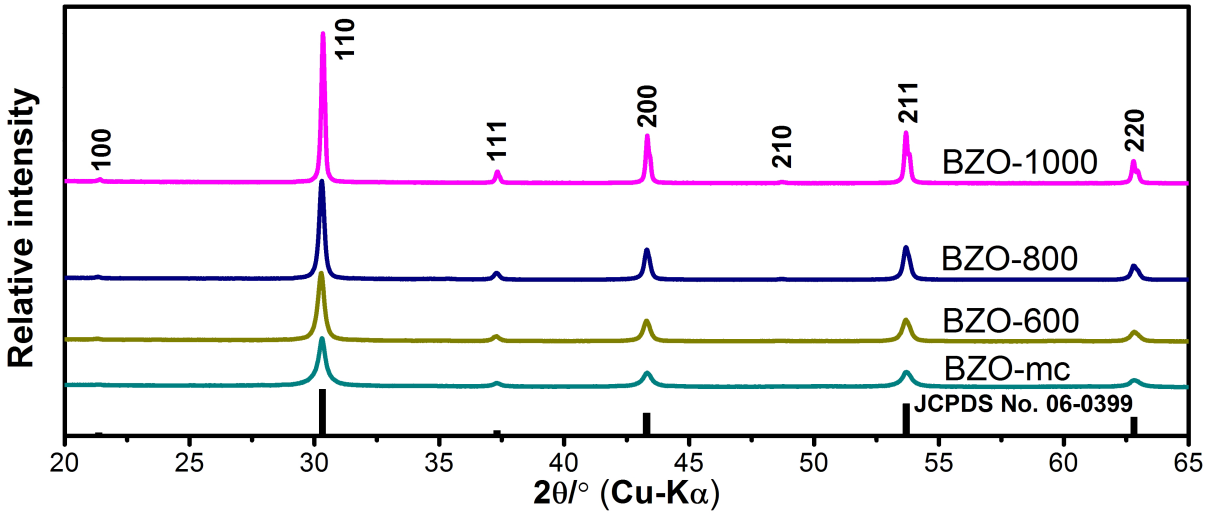

Fig. S4 (A) Elongated XRD patterns of the typical BZO-mc, BZO-600, BZO-800 and BZO-1000 XRD peaks. The intensity of all the peaks increased simultaneously with the elevated temperature.

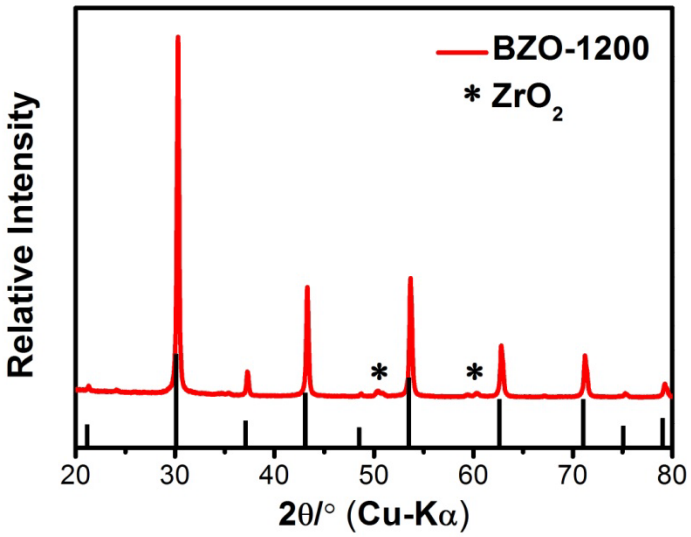

Fig. S5 XRD patterns of the sample BZO-1200. Impurities ZrO_2 will form in the $BaZrO_3$ samples when heated at 1200 °C. In principle, the H_2 production rate can be further increased by calcinating the $BaZrO_3$ mesocrystal hollow nanospheres at an even higher temperature. However, impurities ZrO_2 will form in the $BaZrO_3$ samples when heated at 1200 °C or higher. $BaZrO_3$ hollow nanospheres and these impurity components may form heterojunction structures to enhance their photocatalytic activity, which is however not within the scope of this study.

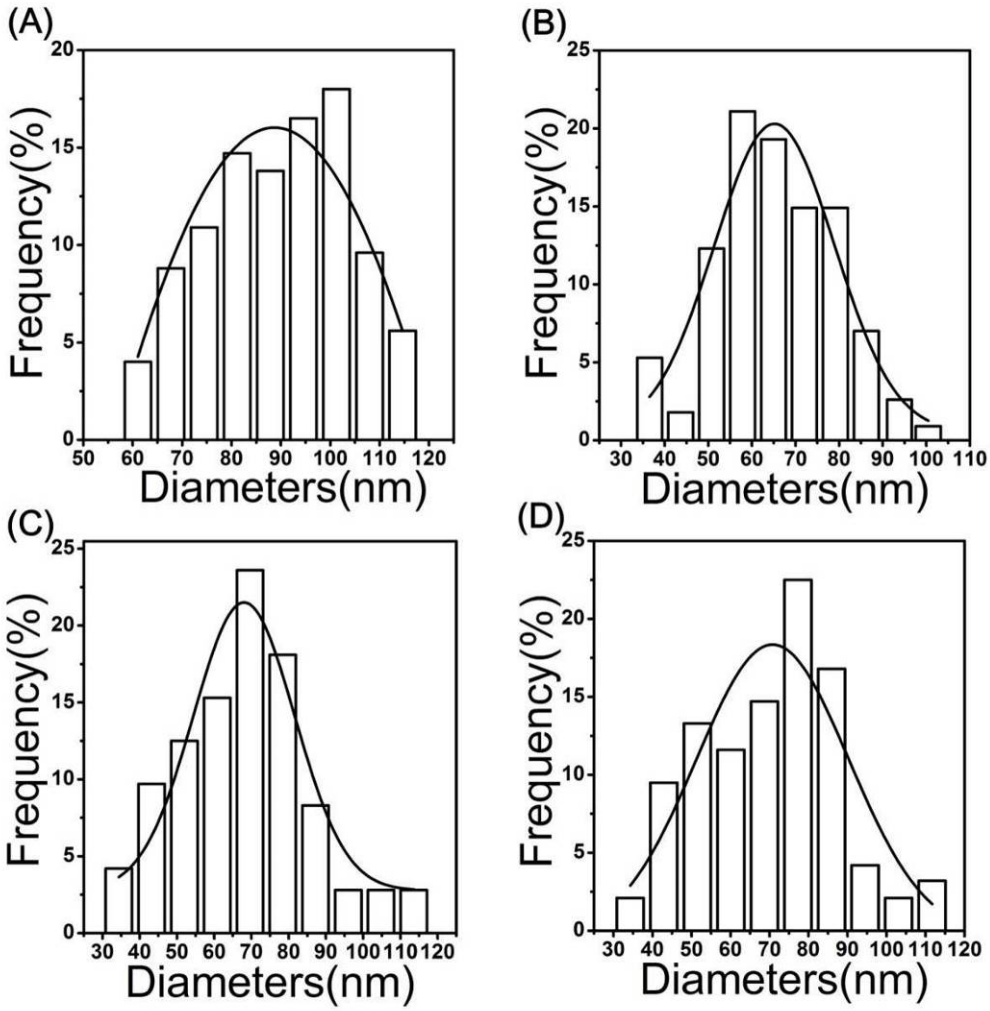

Fig. S6 Particle size distribution of the (A) BZO-mc, (B) BZO-600, (C) BZO-800 and (D) BZO-1000.

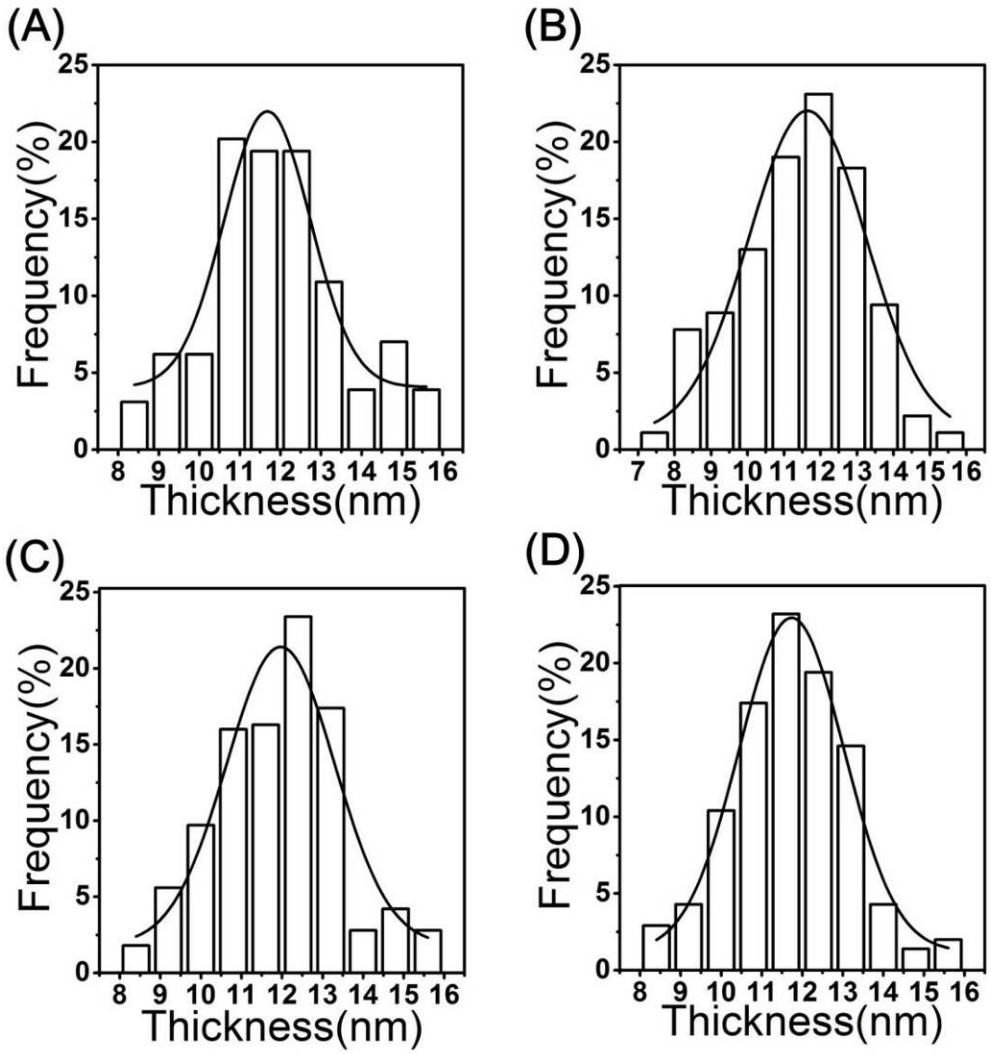

Fig. S7 Shell thickness distribution of the (A) BZO-mc, (B) BZO-600, (C) BZO-800 and (D) BZO-1000.

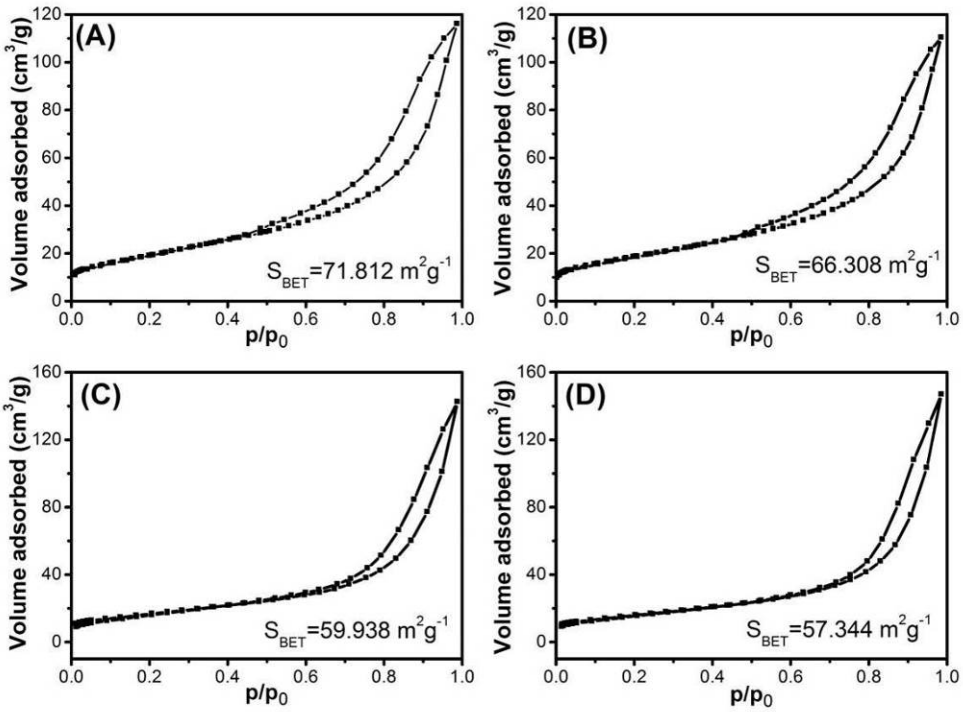

Fig. S8 Nitrogen adsorption–desorption isotherms of the (A) BZO-mc, (B) BZO-600, (C) BZO-800 and (D) BZO-1000. The specific surface area of BZO-mc is 71.812 $m^2 \cdot g^{-1}$. After calcination, the specific surface area of these samples slightly decreased from 66.308 via 59.938 $m^2 \cdot g^{-1}$ to 57.344 $m^2 \cdot g^{-1}$ with increased calcination temperature.

Table S1. Comparison of the photocatalytic hydrogen evolution with different sacrificial electron donors.

Sample	None sacrificial reagent [mmol·h^{-1}g^{-1}]	Methanol [mmol·h^{-1}g^{-1}]	Ethanol [mmol·h^{-1}g^{-1}]	Triethanolamine [mmol·h^{-1}g^{-1}]	Na_2S/Na_2SO_3 [mmol·h^{-1}g^{-1}]
BZO-ref	0.021	0.064	0.059	0.109	0.152

Na_2S/Na_2SO_3 pair was the best sacrificial electron donor to give a very high H_2 evolution rate as compared with none sacrificial reagent and other sacrificial electron donors, including methanol, ethanol and triethanolamine. The reason for why the none sacrificial reagent BZO-ref photocatalytic hydrogen evolution difference from the reference (S2) was that the Xe lamp light sourse we used is not the same as the 400 W high-pressure Hg-lamp in reference (S2).

The S^{2-} could seize the holes effectively and produce S_2^{2-}, which was in turn renewed to S^{2-} by SO_3^{2-}. The reaction mechanism in the presence of S^{2-}/SO_3^{2-} as sacrificial reagent is described by equations 1~6:

photocatalyst + hν → $h^+ + e^-$ (1)

$2e^- + 2H_2O \rightarrow H_2 + 2OH^-$ (2)

$SO_3^{2-} + 2OH^- + 2h^+ \rightarrow SO_4^{2-} + 2H^+$ (3)

$2S^{2-} + 2h^+ \rightarrow S_2^{2-}$ (4)

$S_2^{2-} + SO_3^{2-} \rightarrow S_2O_3^{2-} + S^{2-}$ (5)

$SO_3^{2-} + S^{2-} + 2h^+ \rightarrow S_2O_3^{2-}$ (6)

Table S2. Photocatalytic hydrogen evolution of $BaZrO_3$ hollow nanospheres.

Sample	Calcination [°C]	Shell thickness [nm]	Evolution rate [mmol·h^{-1}g^{-1}]	Nomalized rate[a] [μmol·h^{-1}g^{-1}m^{-2}]
BZO-mc	-	8-16	0.568	7.910
BZO-600	600	7-16	0.658	9.923
BZO-800	800	8-16	0.732	12.212
BZO-1000	1000	8-16	0.833	15.526

a The normalized H_2 evolution rates vs surface areas

Table S3. Comparison of the XRD peak ratio of (110)/(111) for the samples BZO-mc, 600, 800 and 1000.

Peak ratio	BZO-mc	BZO-600	BZO-800	BZO-1000
(110)/(111)	13.15	13.50	13.36	13.55

The XRD peak ratio of (110)/(111) for the samples BZO-mc, 600, 800 and 1000 remained almost unchanged, excluding the effect of specific crystals facets on the photocatalytic activity.

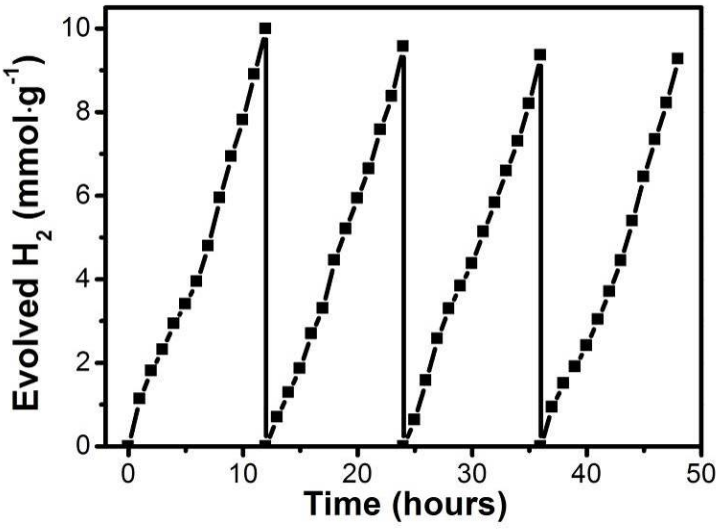

Fig. S9 Time course of photocatalytic H_2 production over used BZO-1000. The reaction was conducted under solar light irradiation (1.5 times in intensity) in aqueous solution containing Na_2S and Na_2SO_3 as sacrificial reagents. The reaction system is pumped to remove the H_2 inside every 12 hours for starting another circle of catalytic reaction. There was a slight loss of the H_2 production in the second circle because of the continuous consumption of the sacrificial reagents of Na_2S/Na_2SO_3. However, the H_2 production rate of BZO-1000 hollow nanospheres after the fourth run (48 h) could still retain ca. 92.8% of that of fresh sample. These results reveal the excellent chemical stability and anti-photocorrosion capability of the BZO-1000 hollow nanospheres in the current photocatalytic system. It is the excellent thermal and chemical stability of the $BaZrO_3$ hollow nanospheres that supply us a flat form to investigate the direct connection between the crystallinity and photocatalytic activity.

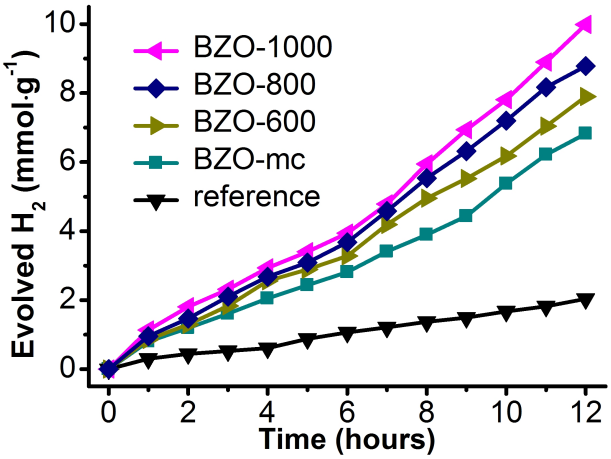

Fig. S10 Typical reaction time course of H_2 production of the BZO-mc, BZO-600, BZO-800 BZO-1000 and reference $BaZrO_3$ bulk sample respectively. For the comparison under the same evalution condition, we prepared the reference $BaZrO_3$ bulk sample according to the Pechini-type process based on reference (S2). The results indicated the photocatalytic activity of BZO-1000 is five times higher than that of the reference $BaZrO_3$ bulk sample.

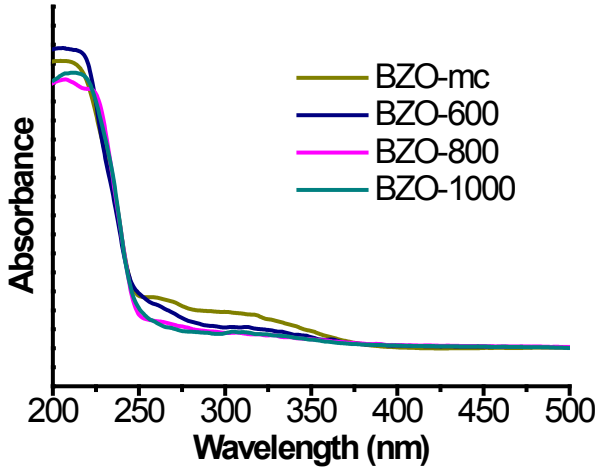

Fig. S11 UV-vis absorption spectra of the BZO-mc, BZO-600, BZO-800 and BZO-1000. The broad band (250~500 nm) may originated from the surface defects of $BaZrO_3$.[(S3)] After the calcinations process, the broad band (250~500 nm) absorption of $BaZrO_3$ decreased obviously, indicating high temperature will remove the surface defects.[(S4)]

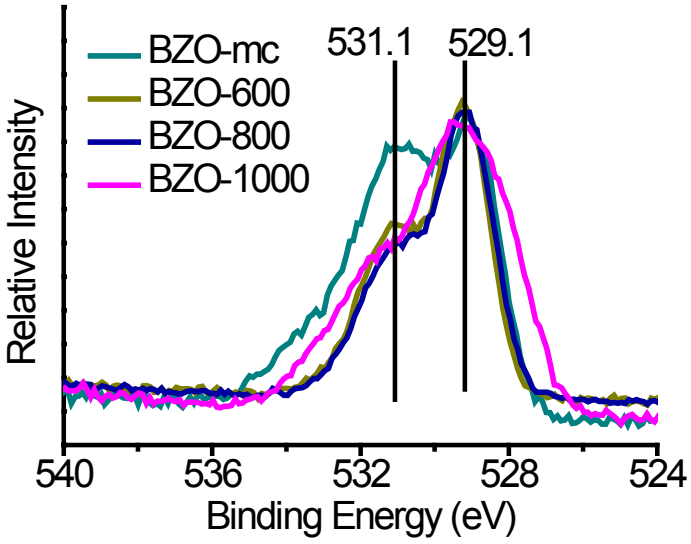

Fig. S12 Normalized XPS O1s spectra of the BZO-mc, BZO-600, BZO-800 and BZO-1000 respectively. The peak at 529.1 eV is associated with the oxygen atoms in the lattice. The peak at 531.1 eV is attributed to the O^{2-} ions in the oxygen-deficient regions, the intensity of which reveals the concentration of oxygen defects in the matrix of $BaZrO_3$.[S5-S7]

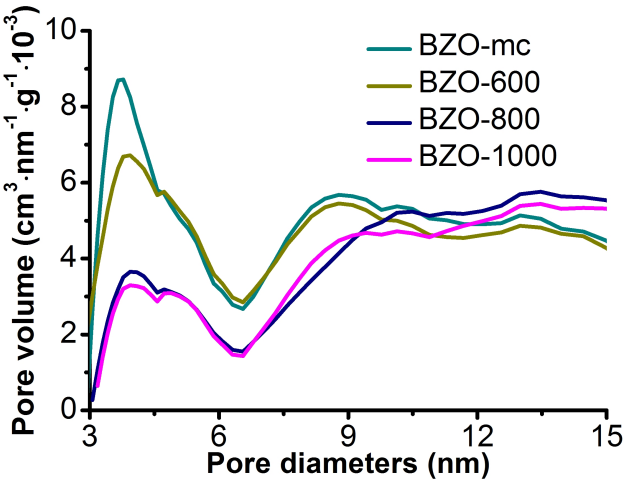

Fig. S13 Pore size distribution of the BZO-mc, BZO-600, BZO-800 and BZO-1000 respectively.

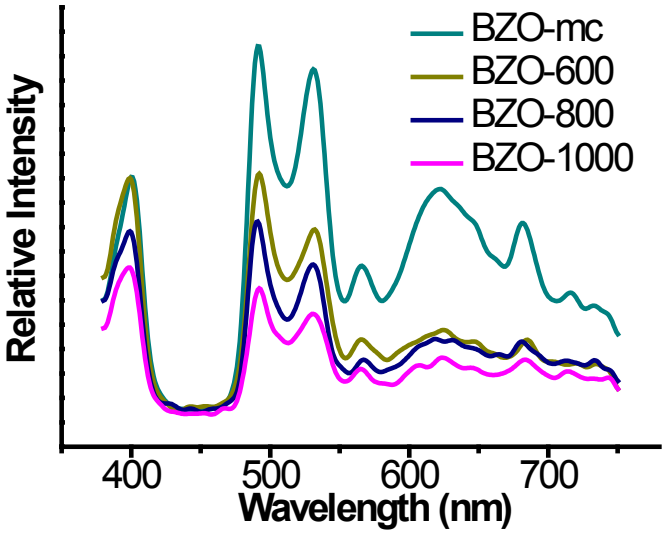

Fig. S14 Photoluminescence spectra under 254 nm excitation of the BZO-mc, BZO-600, BZO-800 and BZO-1000 respectively. The PL spectra band from 375 to 425 nm were the bandgap emissions and the band from 470 to 750 nm were associated with the defect-related emissions. It is clear that the relative intensity of the samples decreased with the calcinations temperature. This observation unambiguously revealed the effect of the crystallinity on the charge separation.

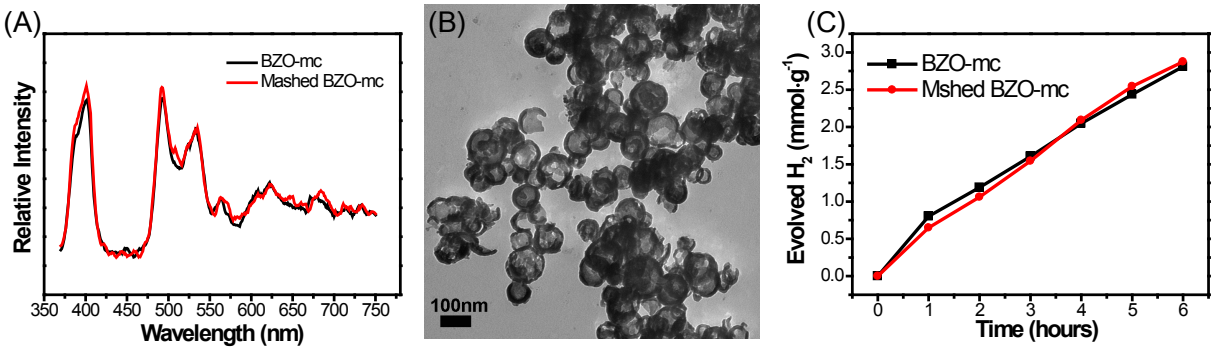

Fig. S15 (A) Fluorescent intensity comparison between the BZO-mc and mashed BZO-mc samples (254 nm excitation). (B) The TEM image of the mashed BZO-mc samples. (C) Typical reaction time course of H_2 production of the BZO-mc and Mashed BZO-mc. In order to exclude the effect of broken shells, we prepared a control sample by mashing the original BZO-mc sample without heat treatment. The PL spectra and the band gap emission (375-425 nm) of the two samples exhibited no obvious change. More importantly, the photocatalytic activity was also not changed obviously (Fig. S15c). Therefore, a tiny amount of broken spheres will not significantly change the photocatalytic properties.

REFERENCES

(S1) Z. H. Dong, T. N. Ye, Y. N. Zhao, J. G. Yu, F. Q. Wang, L. L. Zhang, X. B. Wang, and S. K. Guo, *J. Mater. Chem.*, 2011, **21**, 5978.

(S2) Y. P. Yuan, X. L. Zhang, L. F. Liu, X. J. Jiang, J. Lv, Z. S. Li and Z. G. Zou, *Int. J. Hydrogen. Energ.*, 2008, **33**, 5941.

(S3) W. Chen, Z. G. Wang, Z. J. Lin and L. Y. Lin, *J. Appl. Phys.*, 1997, **82**, 3111.

(S4) J. Koomen, *Solid State Eletron.*, 1971, **14**, 571.

(S5) W. P. Sun, M. F. Liu and W. Liu, *Adv. Energy Mater.*, 2013, **3**. 1041.

(S6) Y. D. Zhu, M. Y. Li, H. Zhou, Z. Q. Hu, X. L. Liu, X. L. Fang, B. Sebo, G. J. Fang and X. Z. Zhao, *J. Phys. D: Appl. Phys.*, 2012, **45**, 375303.

(S7) A. Younis, D. Chu and S. Li, *J. Phys. D: Appl. Phys.*, 2012, **45**, 355101.